Role of applied bias and tip electronic structure in the scanning tunneling microscopy imaging of highly oriented pyrolytic graphite

G. Teobaldi,[1,*] E. Inami,[2] J. Kanasaki,[2] K. Tanimura,[2,†] and A. L. Shluger[3,4,‡]

[1]*Stephenson Institute for Renewable Energy and Surface Science Research Centre, Department of Chemistry, University of Liverpool, L69 3BX Liverpool, United Kingdom*

[2]*The Institute of Scientific and Industrial Research (ISIR), Osaka University, Mihogaoka 8-1, Ibaraki, Osaka 567-0047, Japan*

[3]*Department of Physics and Astronomy, University College London, Gower Street, WC1E 6BT London, United Kingdom*

[4]*WPI-AIMR, Tohoku University, 2-1-1 Katahira, Aoba, Sendai, 980-8577, Japan*

(Received 3 October 2011; revised manuscript received 6 December 2011; published 27 February 2012)

Controlled scanning tunneling microscopy (STM) experiments and first-principles simulations show that applied bias can significantly affect the topographic STM contrast of highly oriented pyrolytic graphite (HOPG) measured with W tips in the pure tunneling regime. Depending on the magnitude and polarity of the bias, both the hexagonal and triangular structures were imaged with the same stable tip. Statistical analysis of the experimental data reveals an enhancement of the corrugation amplitude for small negative biases and the occurrence of different contrast reversals at positive biases, whereby the relative brightness of primary and secondary image features is inverted with respect to that for negative biases. Simulations of HOPG imaging with three different W-tip models explain these findings on the basis of tip-convolution effects governed by the subtle interplay of the tip electronic states with different angular and magnetic moments and vacuum decay lengths. Finally, the calculated library of image contrasts and corrugation amplitudes allows us to rationalize the large variety of, sometimes contrasting, STM data on the basis of effects that different tip terminations, compositions, and sharpness have on the STM imaging of HOPG.

DOI: 10.1103/PhysRevB.85.085433 PACS number(s): 81.05.uf, 07.05.Tp, 68.37.Ef

I. INTRODUCTION

Highly ordered pyrolytic graphite (HOPG) is one of the most extensively used substrates in scanning tunneling microscopy (STM) and is routinely used as a standard for STM calibration.[1] Carbon atoms in individual layers of HOPG are arranged into a honeycomb pattern and separated by interatomic distances of 1.42 Å. The individual layers, or graphene sheets, are weakly bound together by van der Waals (vdW) forces and are stacked according to an $ABAB$ sequence. The HOPG stacking sequence creates two nonequivalent atomic sites, which are usually referred to as α and β [Fig. 1(a)]. While the α site is sandwiched between two C atoms belonging to the adjacent layers, the β atoms face the center of the honeycomb structures (hollow, h site) of the neighboring layers.[2]

The major advantages behind HOPG popularity as a substrate are the possibility to easily create extended (up to μm-sized) atomically flat terraces via cleavage,[3] and to straightforwardly obtain atomically resolved STM images in vacuum, atmospheric, and liquid environments.[4] The relatively high stability of HOPG makes it an ideal substrate also for STM investigations of adsorbed molecules,[5,6] biomolecules,[7,8] and catalytically active metal clusters.[9,10] These features make our understanding and controlling of STM imaging mechanisms of HOPG crucial for research of technologically relevant graphite-[11–16] and graphene-based materials[17–21] as well as for investigations of biomaterials,[7,8] novel catalysts,[9,10] and other energy relevant materials .[22]

Extensive STM investigations of HOPG carried out over the years have evidenced several anomalous features, the incomplete understanding of which has so far hampered direct and straightforward interpretation of STM images of HOPG. One such feature is the giant STM contrast corrugation, which is sometimes recorded for HOPG. This phenomenon has been qualitatively explained in terms of tip-contamination effects[4] and mechanical interaction between the surface atoms and the STM tip.[23,24] Another peculiar feature of HOPG imaging is anomalously large-scale periodic patterns with hexagonal symmetry.[25,26] These superperiodic features generally occur in regions with observable boundaries, and have been rationalized in terms of Moiré patterns originated by the rotational misorientation of the top graphite layer relative to the underlying layers.[27,28]

In spite of these successes, crucial features of STM imaging of HOPG are still poorly understood. In particular, almost all STM images acquired at low sample bias show a hexagonal arrangement of bright features separated by 2.46 Å (*triangular* pattern from now on) instead of a *honeycomb* pattern with 1.42 Å [the α-β bond length, see Fig. 1(a)] distance between bright features. Since the (0001) HOPG surface has two symmetry nonequivalent types of atoms in the unit cell [α and β atoms; Fig. 1(a)], resulting in two sublattices with the same 2.46 Å interatomic distance, the appearance of the triangular pattern has long been associated with selective imaging of only one of the two nonequivalent atoms.[29,30] However, recent simulations suggest that at short (3–4 Å) tip-surface distances, and accordingly large current values, the triangular pattern is pinned on neither the α nor the β atoms, but on the hollow (h) site instead.[31]

Thus, despite extensive investigations, the debate on the interpretation of HOPG images is far from being settled. The controversy spins mainly around three points: (i) the assignment of the bright (and dark) contrast features imaged in the triangular pattern to the HOPG lattice sites; (ii) the physical mechanisms leading to imaging of only one sublattice in the triangular pattern; and (iii) the STM conditions required

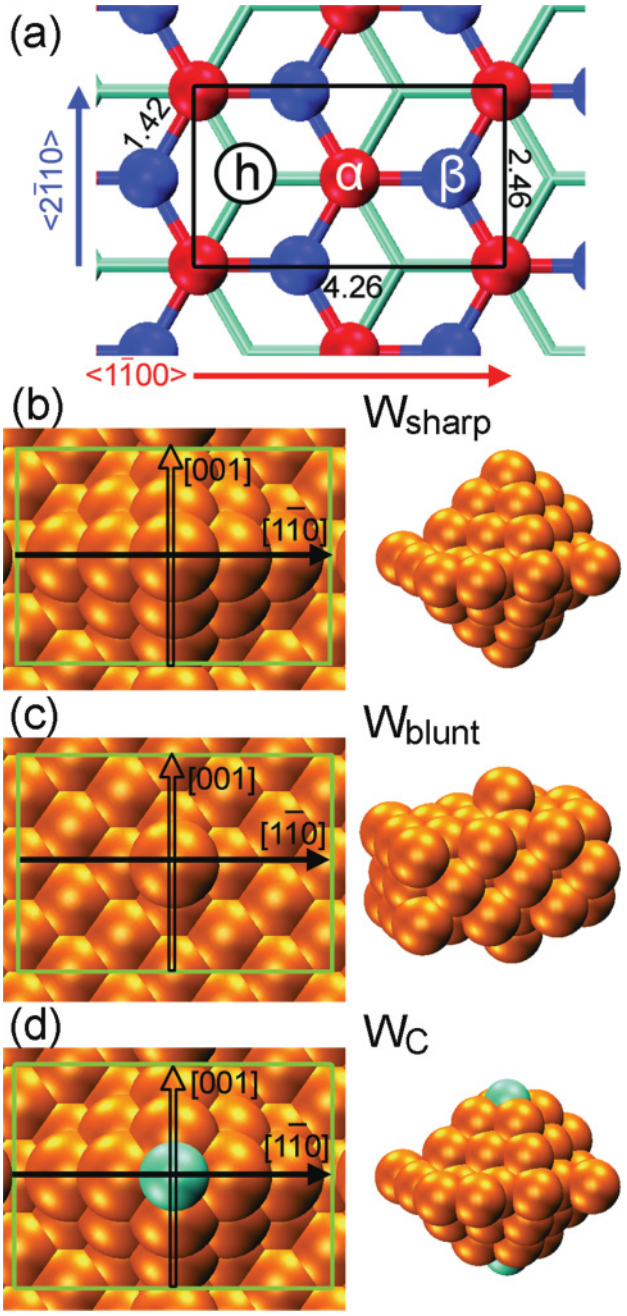

FIG. 1. (Color online) (a) Top view of the adopted seven-layer orthorhombic HOPG slab. The topmost α and β atoms are shown as red (gray) and blue (dark gray) spheres and labeled accordingly. The hollow (h) site is also marked. Distances are in Å. Top (left) and perspective (right) views of the sharp (W_{sharp}), blunt (W_{blunt}), and C-contaminated (W_C) tip models are shown and labeled in panels (b)–(d). W and C atoms in (b)–(d) are displayed as orange (gray) and cyan (light gray) spheres, respectively. In all cases, a rectangle indicates the in-plane extent of the simulations cell, and arrows are used to highlight the considered high-symmetry directions.

for controllable and reversible imaging of the triangular and honeycomb patterns.

In order to settle this controversy and gain better understanding of the STM imaging of HOPG, many experimentalists have sought the hidden atoms by imaging the surface using different scan conditions and tip preparations. In some cases, it has been possible to obtain the honeycomb pattern as a result of nonideal tip effects or mechanical interactions between the tip and the surface. Moriarty and Hughes have shown that the honeycomb pattern can be obtained following an application of a voltage pulse across the tunneling junction and attributed the appearance of this pattern to a tip modification induced by the pulse.[32] By modeling the effect of multiple-apex terminations on the recorded STM imaging, Mizes and Harrison have shown that the occurrence of a double-apex tip can also result in the honeycomb pattern.[33]

In some cases, it has also been possible to observe a transformation between the triangular and honeycomb contrast patterns during repeated scans. These results have been rationalized in terms of the tip-induced sliding of the topmost HOPG layer relative to the underlying layers.[34,35] On the other hand, Wang *et al.* have simultaneously recorded the appearance of both structures using the same tip.[36] STM image acquisition across a domain boundary resulted in the triangular and honeycomb patterns being measured simultaneously on each side of the boundary. Also in this case, the appearance of the honeycomb pattern has been explained in terms of translational displacement of the topmost layer near the domain boundary without any reference to tip-induced effects.[36]

Recently, Cisternas *et al.* have succeeded in controllably observing both the triangular and honeycomb patterns on the same HOPG terrace and clarifying the conditions required for observing both contrasts.[37] The honeycomb structure was resolved by constant-height scanning at sample biases over −200 mV and tunneling currents of 1.5–3 nA. For the same applied bias, and reportedly the same tip termination, a conversion of the honeycomb contrast into the triangular one was obtained by retracting the tip by 1.0 Å further away from the surface. Based on these findings, the authors argued that both the applied bias and the tip-surface distance can have major effects on imaging of HOPG. However, the magnitude of tunneling current used in this study was much larger compared to that routinely used to image HOPG in the same bias range.[29,30,32,34–36,38–40] As a result, and in line with recent suggestions,[31] the mechanical tip-surface interaction could have contributed to the imaging of the honeycomb structure. Furthermore, the conclusions in Ref. 37 are based on images acquired in *constant-height* mode. Therefore, the role of applied bias and tunneling current (i.e., the baseline tip height above the surface) in the HOPG *constant-current* topographic imaging still remains to be addressed.

Apart from extensive experimental investigations, the asymmetry of HOPG contrast has also been the subject of many theoretical studies since the advent of STM. The first interpretation of the HOPG asymmetry stems from the work of Tománek *et al.*[41,42] This theory explains the asymmetry on the basis of the higher (lower) local density of states (LDOS) for the β (α) atoms close to the Fermi energy of HOPG, which causes the β atoms to appear brighter than the α atoms at low biases. This leads to the appearance of a (β-centered) triangular structure. The theory also predicts that the asymmetry should be independent of the bias polarity and disappear for large-bias voltages, leading to formation of the honeycomb pattern. Although successful in accounting for the triangular appearance of HOPG at low-bias voltages,[29,30,38]

this theory fails to explain the experimental persistence of the triangular pattern at higher voltages.[37,39] It is also seriously challenged by the existence of low-bias images showing a honeycomb pattern.[32,36,37] Last but not least, this theory can be hardly reconciled with the experimentally measured reversals of STM contrast as a function of the applied bias[39] and the tip height above the surface.[40] Effects related to the tip electronic structure[39] and surface deformation[40] have been put forward in order to qualitatively explain these apparently surprising findings.

Importantly, despite early suggestions based on simplistic tip models,[43–45] most of the more recent theoretical studies of HOPG STM imaging[37,38,41,42,46,47] have been carried out within the Tersoff-Hamann approximation,[48] neglecting effects of the tip electronic structure on the STM image. One exception is the recent work reported in Ref. 31 where more advanced calculations were carried out for only one bias value. Thus, to the best of our knowledge, the combined effect of the tip electronic structure and applied bias on the asymmetry of HOPG images has not been addressed yet. Therefore, the experimental and theoretical understanding of STM imaging of one of the structurally simplest and best-characterized surfaces is still far from being complete.

Further progress in our understanding of STM imaging of HOPG at both small and large biases requires systematic, controlled, and reproducible study of the dependence of HOPG STM contrast on the tip preparation and applied bias. Achieving such an understanding is timely in view of the increasingly broad use of STM for characterizing the structure and electronic properties of nanoengineered HOPG,[11–16] multilayer graphene,[17] HOPG-supported biomolecules,[7,8] and catalysts.[9,10,22]

Therefore, the main aim of this paper is to investigate whether by using a stable tip one can obtain different constant-current topographic images of HOPG as a function of the applied bias. In addressing this question, we would like to avoid as much as possible any effects caused by short tip-surface separation and mechanical interaction. To this end, we record and statistically analyze several HOPG topographic images acquired between -1 and $+1$ V using a stable W tip at 90 K. To minimize differences in the baseline tip-surface distance, in each case the topographic scanning conditions were determined on the basis of a prerecorded current-bias (I-V) calibration, which was also used as a standard for the tip control. For the sake of comparison, all the STM images in this study were acquired in constant-current mode as this is the approach predominantly used in the literature for graphite and graphene-based materials.[18–21] Statistical analysis of the experimental data reveals a profound effect of the applied bias on the topographic contrast of HOPG. Depending on the applied bias, we observe both the honeycomb and triangular structures. Notably, we also observe different contrast reversals between the triangular and honeycomb patterns at positive biases.

We analyze the experimental data using first-principles simulations accounting for the electronic structure of six different representative tip models. In line with the experimental findings, we show that the effect of the electronic structure of the tip on the HOPG imaging depends on the applied bias. Importantly, we also find that the tip-induced effects strongly depend on the tip composition and sharpness. Aside from rationalization of the measured topographic images, corrugations, and I-V curves, the simulations allow us to reconcile diverse, and sometimes contrasting, results that have been published in the rich literature on HOPG.

The paper is organized as follows. Following the description of the experimental and theoretical methods in Sec. II, we present the experimental results in Sec. III A. The electronic structures of the surface and tip models are briefly presented in Secs. III B and III C, respectively. Following considerations of the effect of the tip-surface distance on the tip-surface interactions (Sec. III D), the calculated STM appearance of HOPG for the considered models is reported in Sec. III E. The experimental and theoretical results are compared and discussed in Sec. IV in relation to the previously published data. Section V summarizes and concludes the paper.

II. METHODS

A. Experiments

The experiments were performed using a low-temperature scanning tunneling microscope (LT-STM) from UNISOKU with a base pressure of 5×10^{-11} Torr. The HOPG samples (ZYA grade) were prepared in air by peeling of some top graphene layers with an adhesive tape before transfer into the ultrahigh vacuum chamber. The STM and scanning tunneling spectroscopy (STS) measurements were performed at 90 K using electrochemically etched tungsten (W) tips. Wide defect-free terrace regions were fully characterized. At the beginning of the measurements, tips were scanned over wide terraces repeatedly *for days* in order to get them stabilized: this procedure was crucial for obtaining atomically resolved images during repeated scans for hours. Using the thus prepared tips, we measured constant-height tunneling current versus voltage (I-V) spectra by sweeping the sample bias voltage from -1.0 to 1.0 V, with the feedback circuit opened. The measurements were carried out at the tip-surface distance, which was determined by the initial set current at 450 pA at the sample bias voltage of -300 mV. Since the vertical drift rate in our system was less than 0.5 pm s^{-1}, the change of tip-surface distance during the spectrum acquisition (1.1 s) was estimated to be 0.6 pm. The topographical images were then obtained at different bias voltages in the range between -1.0 and $+1.0$ V. To minimize differences in the tip-surface distance during scans at different biases, the tunneling current of each topographic scan was set to the same value as in the pristine I-V calibration.

To address the dependence of the measured topographic corrugation on the applied bias, we performed statistical analysis of the topographic images using a procedure described in Ref. 49.

B. Computational details

The graphite surface was modeled as a seven-layer AB-stacked 1×1 orthorhombic slab of 2.467×4.273 Å^2 in-plane extension [Fig. 1(a)]. Given the negligible surface relaxation measured by electron diffraction,[50] and calculated by vdW-corrected density functional theory (DFT),[51,52] the interlayer distance was kept fixed at its experimental value (3.35 Å).[53]

Following Refs. 54 and 55, a sharp W tip (W_{sharp}) was modeled as a symmetric seven-layer W(110) bipyramid with a 3×3 (13.534×9.57 Å^2) in-plane periodicity [Fig. 1(b)]. To investigate possible effects due to the tip-apex sharpness, we considered also a complementary blunt tip (W_{blunt}) constituted by three periodically repeated W(110) layers with two adatoms on each side [Fig. 1(c)]. The carbon-contaminated W_C tip [Fig. 1(d)] was created by substituting each of the W apex atoms of the W_{sharp} tip by carbon atoms. The z coordinates of the three (two) outermost layers of the W_{sharp} and W_C (W_{blunt}) tip models were optimized until the atomic forces were smaller than 0.02 eV Å^{-1}.

Both the graphite slab and the tip models were simulated within the generalized gradient approximation Perdew-Burke-Ernzerhof (GGA-PBE) (Ref. 56) projector augmented wave (PAW) scheme as implemented in the plane-wave VASP code.[57,58] The surface Brillouin zones of the graphite slab and of the tip models were sampled with a grid of 273 and 35 symmetry irreducible (SI) k points, respectively. These k-point grids were checked against augmented grids of 322 and 48 SI k points, respectively. In both cases, we found the original grids to be sufficiently dense to yield the results within the Tersoff-Hamann and Bardeen models (see the following) converged for all the considered energy range of ± 1 eV around the Fermi level. The electronic structures of both the graphite slab and tip models were calculated using a 700-eV plane-wave cutoff.

The adsorption energy of the apex-atom (E_{ads}) was calculated as

$$E_{ads} = \tfrac{1}{2}(E_{tip} - E_{blunt} - 2E_{apex}), \qquad (1)$$

where E_{tip} and E_{blunt} are the energies of the symmetrically optimized tip models with and without the (two) apex atoms, respectively. E_{apex} refer to the energy of one isolated apex atom in the vacuum.

The STM imaging of the graphite surface was simulated using both the Tersoff-Hamann[48] (TH) and Bardeen[59] methods, as implemented in the BSKAN code.[60–62] Further details on the STM simulations can be found in Ref. 49.

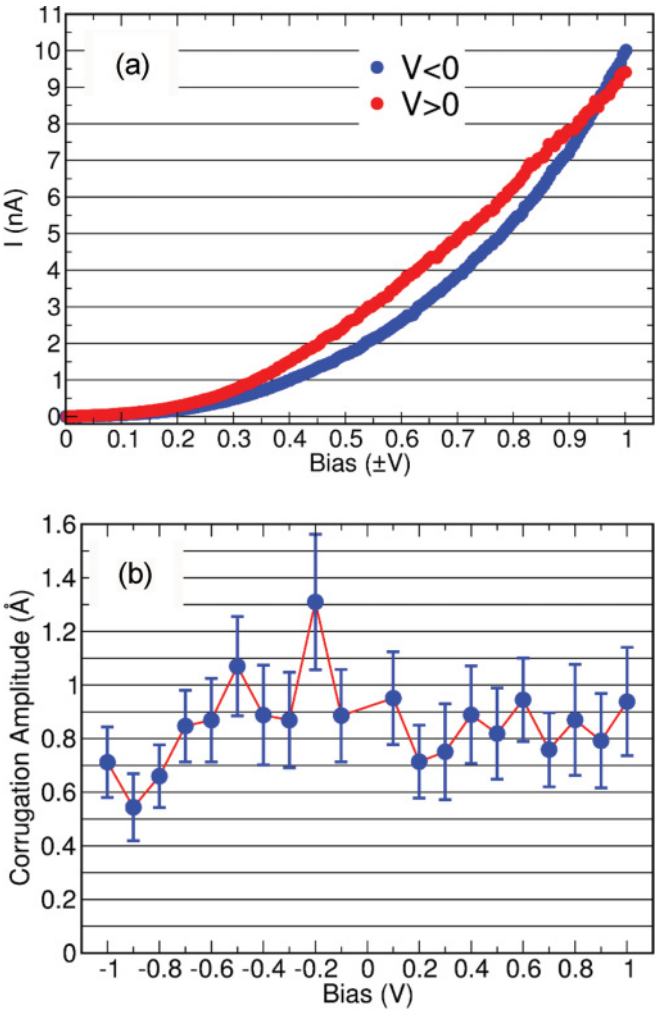

FIG. 2. (Color online) (a) Average I-V calibration (set-point conditions: bias= −0.3 V, $I = 0.45$ nA) for negative (V< 0) and positive (V> 0) applied biases. (b) Average topographic corrugation amplitude (and corresponding error bars) as a function of the applied bias (see text for discussion).

III. RESULTS

A. Experimental W-tip STM imaging of HOPG

As discussed above, both the applied bias and the tip height above the surface can greatly affect the STM image of HOPG probed with W tips.[31,37,39,40] To consistently investigate this effect and address how the relative brightness of HOPG imaged with the same stable tip is affected by the applied bias, we carried out low-temperature (90-K) STM measurements at different biases in the range between −1.0 and +1.0 V using W tips.

Prior to the topographic imaging, and in order to assess the tip stability during the measurements, we recorded constant-height current-voltage (I-V) calibration curves for the stabilized tip. I-V curves were recorded above three different surface sites within a wide defect-free region. The tip height above the surface was set at a sample bias of −0.3 V and a tunneling current of 450 pA. For each considered site, the corresponding I-V curves were measured 10 times and for the same tip-surface distance as determined by the initial (−0.3 V, 450 pA) set point. This accounts for 30 I-V calibration curves, the average of which is reported in Fig. 2.

The averaged I-V curve shows a slightly asymmetric parabolic behavior with slightly larger (10%) currents (hence conductance) for positive bias. By following the same tip preparation as previously described (see Sec. II), it was possible to reproducibly recover I-V calibration curves very similar to those shown in Fig. 2. Therefore, the I-V calibration in Fig. 2 was adopted as a standard to control the tip stability, which was found to be the same before and after the acquisition of all the considered images. Control over the tip stability together with the I-V calibration in turn allowed us to minimize differences in tip-surface distances between topographic images acquired at different biases in the range between −1.0 and 1.0 V.

Figure 2(b) reports the average topographic corrugation amplitude [$\bar{A}$, see Eq. (S-7) in 49] as a function of the applied bias. Within the experimental dispersion [Eq. (S-8) and Table S-1 in Ref. 49], we find $\bar{A}$ to depend on the applied bias. While relatively constant (0.8–0.9 Å) from −0.1 to 1.0 V, the average

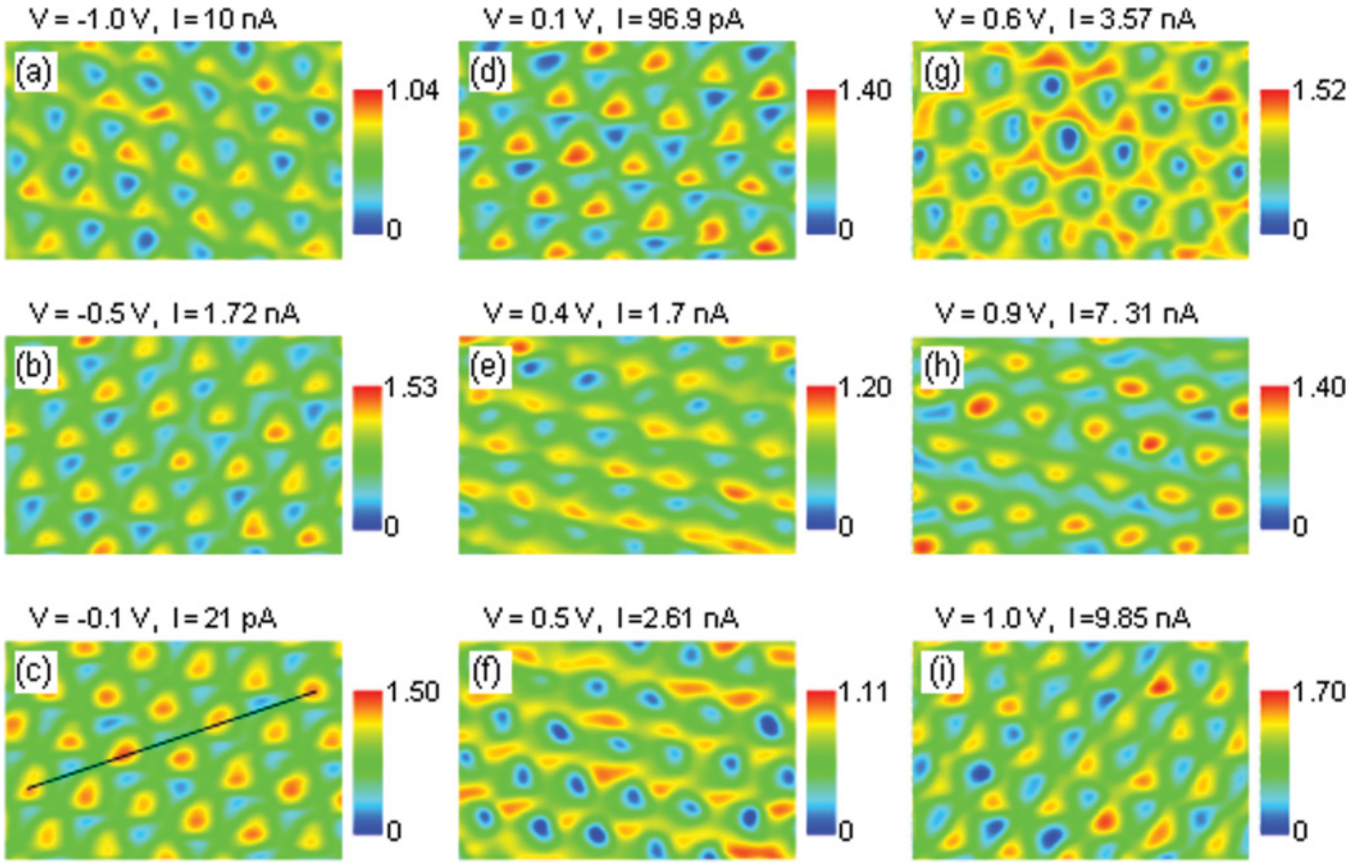

FIG. 3. (Color online) Selected experimental topographies of HOPG at different applied biases in the range between −1 V (a) and +1 V (i). To minimize differences in the tip-surface distance, the tunneling conditions (reported on each panel) have been set according to the I-V calibration standard in Fig. 2(a). The black line in (c) marks the assigned $\langle 1\bar{1}00\rangle$ HOPG direction. Topographic maxima and minima are shown as light gray (red) and dark gray (blue) spots, respectively. In each panel, the labeled color scale reports the *relative* tip-surface distance (Å). Note that, due to the unknown value of the absolute tip-surface distance, only a comparison between differences in *relative* tip-surface distances (i.e., *corrugation amplitudes*) between images acquired at different biases is meaningful.

corrugation increases to 1.3 and 1.1 Å for biases of −0.2 and −0.5 V, respectively. Further reduction of the applied bias below −0.7 V leads to a decrease of the measured corrugation to 0.7–0.5 Å.

Representative topographic images acquired in the considered bias range are displayed in Fig. 3. Topographic images recorded at bias voltage of −0.1 V show the previously reported[29,30,37–40,66,67] triangular pattern [Fig. 3(c)]. As the bias is gradually decreased to −1.0 V, the image is also gradually changed from a triangular into a honeycomb pattern where two different atomic sites are clearly identified [Figs. 3(a) and 3(b)]. Application of a small positive bias [0.1 V, Fig. 3(d)] also yields a triangular pattern, in close agreement with the −0.1 V results. Increasing the bias to the 0.4–1.0 V range results in the contrast change from triangular to honeycomb [Figs. 3(e)–3(i)]. However, for biases larger than 0.7 V, and despite the persistence of atomic resolution, we recorded an overall increase of a scratch-type noise or the change of the corrugation magnitude. Nevertheless, even after such relatively noisy images, when the bias was changed to 0.1 V, it was possible to recover the expected triangular structure, which confirms the overall stability of the tip.

Despite several attempts, the W tip proved to be not stable enough to allow for multibias type[39] imaging of the HOPG surface. As a result, the experimental topographies were obtained independently for each applied bias. Unfortunately, despite the application of drift corrections, this prevents us from unambiguous comparison of the absolute positions of the topographic features with respect to the underlying atomic-lattice structure for images acquired at different biases.

However, assuming that the brightest topographic features lie along a generic $\langle 1\bar{1}00\rangle$ direction passing through the α, β, and h sites [Fig. 1(a)], it is nevertheless possible to identify at least the $\langle 1\bar{1}00\rangle$ vector in the images as the direction along which the topographic minima (or maxima) are separated by ∼4.26 Å, i.e., three times the α-β ($=h$-$\alpha = \beta$-h) distance [Fig. 1(a)]. This assumption is corroborated by our results (see below) as well as by independent simulations including the STM tip,[31] and previous multibias experimental measurements.[39]

If this assignment is correct, the only variable left uncertain is the α-β-h or h-β-α orientation of the $\langle 1\bar{1}00\rangle$ scanline [see Fig. 1(a)]. To determine that, we used the results of our simulations in the Bardeen approximation at −0.1 V. As shown below, regardless of the considered orientation of the W-tip model, the simulations suggest that the β atom and h site are the brightest and darkest features of the contrast, respectively [Figs. 9(a)–9(d)]. However, the β-centered feature has an

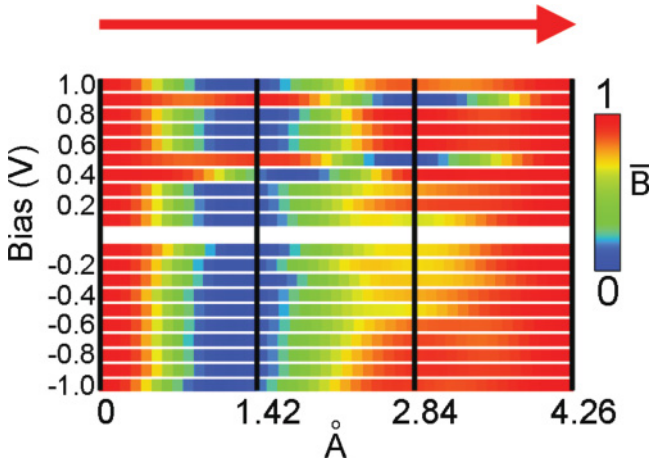

FIG. 4. (Color online) Experimental average relative brightness ($\bar{B}$) profiles along the $\langle 1\bar{1}00\rangle$ maxima-minima-maxima direction as a function of the applied bias. For the sake of comparison, all profiles have been shifted to start with the corresponding brightness maximum ($\bar{B} = 1$). The arrow marks the $\langle 1\bar{1}00\rangle$ direction, as indicated in Fig. 1(a). Note that, with the only exception of the −0.1 V profile, the absolute in-plane position of the topographic features along the scan lines are yet unassigned (see text for discussion).

asymmetric shoulder, which faces the α site. This asymmetry, which is present also in the experimental topographic images [Figs. 3(c) and 4], is used to identify the $\alpha \rightarrow \beta$ direction and hence the α-β-h orientation. In the absence of macroscopic rotations of the sample holder, this orientation should not be inverted between the STM scans at different biases.

We stress that (i) in the absence of direct comparison between the experimental and calculated asymmetries along the $\langle 1\bar{1}00\rangle$ scanline at −0.1 V, it is not possible to unambiguously assign α-β-h direction in the experimental topographies, and (ii) assignment of the (α,β,h) sites in one topography (at −0.1 V in the present case) does not allow rigorous assignment of the HOPG sites in topographies independently acquired at different biases, unless the uncertainty due to the lateral drift between different images is reliably proved to be negligible (<0.1 Å, see also Figs. 9 and 10). These important points have been previously overlooked in several STM investigations[39,68] and significantly complicate comparison between different STM experiments available in the literature.

Once the (instantaneous) $\langle 1\bar{1}00\rangle$ directions have been defined, by knowing the in-plane positions of the topographic minima (m) and maxima (M),[49], it is possible to calculate an average brightness profile [Eq. (S-11) in Ref. 49] for each experimental topography. The resulting contrast map is presented in Fig. 4. To facilitate the comparison between the average brightness profile ($\bar{B}$) at different biases, the profiles have been shifted to start with the corresponding maximum ($\bar{B} = 1$). To the best of our knowledge, this kind of analysis has not been used in previously published STM studies of HOPG.

For the sake of discussion, we introduce the following convention: whenever a secondary maximum with relative brightness ($\bar{B}$) larger than 0.7 appears in the profile, we define the contrast pattern as hexagonal. Conversely, for profiles without secondary maxima or with secondary features darker than $\bar{B} = 0.7$, the corresponding contrast is defined as triangular.

As shown in Fig. 4, for negative biases smaller than −0.6 V, the average contrast progressively changes from a hexagonal pattern into a triangular one (−0.5/−0.1 V). The triangular pattern is found to persist for up to small ($\leqslant$0.3 V) positive biases. However, further increase of the bias above 0.3 V leads to the reappearance of the hexagonal pattern, which is maintained, although with some minor differences in the brightness of primary and secondary features, up to a bias of 1.0 V.

Closer inspection of Fig. 4 reveals another rather interesting point. While for biases between −1.0 and 0.4 V, the secondary maxima or asymmetric shoulders are roughly 1.42 Å on the left of the principal feature (i.e., at scan length of 2.84 Å), at 0.5 V the secondary feature is localized roughly 1.42 Å on the right of the profile maximum (i.e., at scan length of 1.42 Å). Further increase of the bias in the 0.6 V/0.8 V range leads to reappearance of a standard hexagonal pattern (secondary feature on the left of the primary feature), which then is again inverted at 0.9 V (secondary feature on the right of the primary feature), and back-converted to its standard form at 1.0 V. In the absence of macroscopic rotation of the sample and tip holder, these results show unambiguously that the application of 0.5 and 0.9 V biases changes the STM contrast, whereby the relative position of the primary and secondary features along $\langle 1\bar{1}00\rangle$ is inverted. Thus, the tip stability during the topographic acquisition and the results presented in Fig. 4 clearly suggest that the applied bias does significantly affect the STM contrast of HOPG. In the following, we present the results of theoretical simulations of STM images, which shed some light on the mechanism of this effect.

B. Calculated HOPG electronic structure

Prior to considering the effects of the tip electronic structure on the simulated STM appearance of HOPG, we present the main results for the bare surface.

The calculated density of states (DOS) for HOPG [Fig. 5(a)] shows a symmetric and nearly parabolic dispersion around the Fermi energy (E_F). Consistent with the semimetallic nature of HOPG and with previous theoretical results,[41,42,69,70] we recover a practically zero DOS at E_F. The simulated atom-projected DOS (PDOS) for the topmost β atoms (β-PDOS) is consistently larger than for the topmost α atoms (α-PDOS) in an energy window of 0.5 eV around E_F. This difference is, however, noticeably reduced for occupied states more than 0.5 eV below E_F. In addition, the calculated α-PDOS is found to be larger than β-PDOS for energies larger than E_F+0.6 eV. These findings deviate from previous tight-binding results on multilayer graphite slabs, which suggest β-PDOS to be symmetrically larger than α-PDOS to within 0.8 eV around E_F.[41,42,69,70] Our simulations with the augmented 322 k-point grid confirm this deviation from the tight-binding results, which we attribute to the specific parametrization adopted in Refs. 41, 42, 69, and 70.

While useful for the interpretation of the electronic structure at the HOPG surface, the PDOS analysis in Fig. 5(a) does not account for the vacuum decay of the electronic states above the considered surface.[60,61,63–65] To this end, we turn

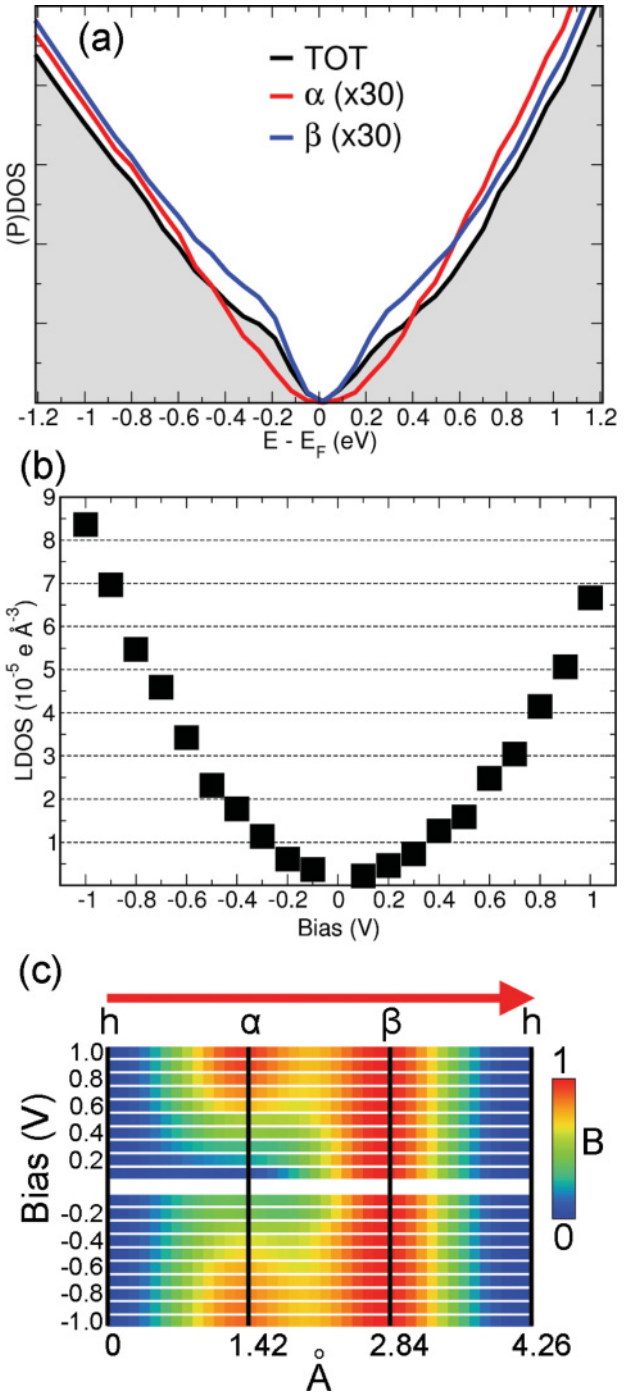

FIG. 5. (Color online) (a) The calculated total (TOT) density of states (DOS) and topmost α- and β-projected DOS (PDOS) of the HOPG slab. (b) The lowest LDOS values in an (xy) plane 3 Å above the HOPG slab as a function of the simulated bias. (c) The relative brightness (B) profiles along $\langle 1\bar{1}00\rangle$ [gray (red) arrow, see also Fig. 1(a)] as calculated from the topographic Tersoff-Hamann imaging of HOPG at the LDOS values displayed in (b).

to the calculated LDOS above the HOPG surface. As noted in Ref. 49, within the TH approximation, the calculated LDOS above the surface [Eq. (S-1)] can be used as a first approximation to the tunneling current.

In line with the DOS dispersion around E_F, also the LDOS above the surface is found to increase rather symmetrically as a function of bias [Fig. 5(b)]. This result stems from the homogenous (π) nature and vacuum decay length of the HOPG electronic states around E_F.[41,42,69,70] To directly compare the LDOS localization above the surface for different energies in the $E_F \pm 1.0$ eV window, we use the brightness parameter (B) introduced in Eq. (S-9).[49] Figure 5(c) shows the B profiles along the HOPG $\langle 1\bar{1}00\rangle$ direction running parallel to the C-C bonds [Fig. 1(a)] as calculated from the topographic Tersoff-Hamann imaging of the HOPG slab. In agreement with the original suggestions of Refs. 41 and 42, and consistent with the calculated PDOS for HOPG [Fig. 5(a)], the B profile of HOPG is dominated by β atoms for relatively small biases of ± 0.4 V. This results in a sharp (β-centered) triangular structure for images acquired in the ± 0.4 V range. However, for biases larger than ± 0.4 V, the brightness of the α atom progressively increases up to 95% of the β-atom brightness, which leads to a hexagonal pattern pinned on the topmost α and β atoms. Also in agreement with previous findings,[41,42] these results are practically independent from the baseline height above the surface in the range between 2 and 7 Å (see Ref. 49, Fig. S-2).

C. Tip electronic structure

The metallic character of the periodic W_{sharp}, W_{blunt}, and C-contaminated W_C tip models results in a nonzero DOS at E_F (Fig. 6 and Fig. S-3 in Ref. 49). For all the considered tip models, the dispersion of the tip-apex atom PDOS around E_F (Fig. 6) suggests that this atom interacts strongly with the rest of the slab and is involved in the metal bonding.

The electronic structure of the tip apex around E_F is dominated by W $5d$ states for the W_{sharp} (W_{blunt}) tips, and by C $2p$ states for the W_C. In line with previous results for atomically sharp tip models,[64,71] the angular- and magnetic-moment-resolved PDOS analyses in Fig. 6 demonstrate different energy-dependent contributions of in-plane $(x,y,xy,x^2\text{-}y^2)$ and out-of-plane (xz,yz,z,z^2) electronic states at the tip apex. Notably, the difference in PDOS spectra for the W_{sharp} and W_{blunt} models demonstrates that the energy-dependent balance of in-plane and out-of-plane contributions at the tip apex strongly depends also on the subapex structure of the tip.

To examine the decay of the tip electronic states away from the tip apex as a function of the sampled energy window, we performed a Tersoff-Hamann analysis [Eq. (S-1) (Ref. 49)] of the considered tip models. We note that for this analysis, we reference the applied bias to the tip (not the sample) and, consequently, occupied (empty) tip states are sampled for positive (negative) biases. The decay of the tip electronic states into vacuum as a function of applied bias is shown in Fig. 6(d). The calculated LDOS values at 3 Å above the tip apex show differently asymmetric behavior for different tip models. This originates from the different energy-dependent balance between fast-decaying in-plane $(xy,x^2\text{-}y^2)$ and slow-decaying out-of-plane states (xz,yz,z^2) at the tip apex. Thus, the larger in-plane $(x^2\text{-}y^2)$ contributions to the occupied states of the W_{sharp} apex [Fig. 6(a)], accounting for a shorter vacuum decay length, result in smaller LDOS values for negative biases. Conversely, the larger out-of-plane (yz,z^2) contributions to the empty states of the W_{sharp} apex [Fig. 6(a)], yielding a longer vacuum decay length, lead to larger LDOS values for

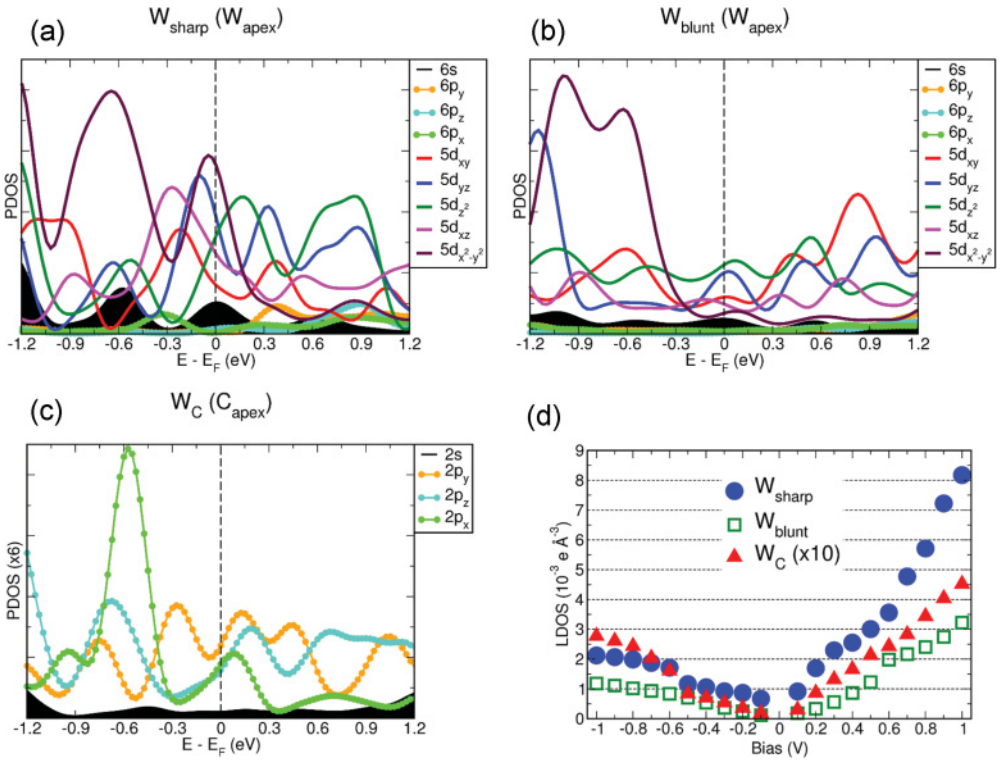

FIG. 6. (Color online) The angular- (s,p,d) and magnetic-moment- $(x,y,z,xy,xz,yz,x^2\text{-}y^2,z^2)$ resolved analysis of the atom-projected density of states (PDOS) at the tip apex for the W_{sharp} (a), W_{blunt} (b), and W_C tip models (c). (d) The calculated lowest LDOS values in an (xy) plane 3 Å above the apex as a function of the applied bias for all the considered tip models.

positive biases. On the other hand, the predominantly in-plane $(xy,x^2\text{-}y^2)$ composition of both occupied and empty states at the W_{blunt} apex [Fig. 6(b)] yields a more symmetric distribution of the LDOS as a function of the applied bias.

To investigate the actual sharpness of the tip models, we next consider the real-space distribution of the electronic states above the tip apex at different biases. Analysis of the tip LDOS and brightness (B) profiles (displayed in Figs. S-4, S-5, and S-6 of Ref. 49 for the interested reader) indicates a rather symmetric distribution of the tip electronic states for both the W_{sharp} and W_{blunt} models. Notably, the calculated full width at half maximum (FWHM) for both W_{sharp} and W_{blunt} tips varies within 2.4 and 2.8 Å, depending on the simulated bias. These values are close to twice the α-β $(= h\text{-}\alpha = \beta\text{-}h)$ distance [1.42 Å, Fig. 1(a)]. Thus, the electronic distributions for the atomically sharp W_{sharp} and W_{blunt} tip models turn out to be rather wide in comparison with the HOPG lattice spacing, suggesting that convolution effects may play an important role in determining the tunneling matrix elements and tunneling current [Eq. (S-3) in Ref. 49]. These effects are qualitatively illustrated in Fig. 7.

In the case of the W_C model, we find the corresponding LDOS distribution and B profile to be more asymmetric, broad, and structured (Fig. S-6 in Ref. 49). This results from the longer vacuum decay length of W $5d$ subapex states with respect to the C-apex $2p$ states and points toward possibly even larger convolution effects in STM images of HOPG acquired with C-contaminated tips.

Thus, both the complicated electronic structure of the tip apex (Fig. 6) and large FWHM of the electronic states at the tip apex with respect to the HOPG lattice spacing suggest that bias-dependent tip-specific effects may prove important for evaluating the tunneling matrix elements $M_{\tau,n}$ [Eq. (S-4) in Ref. 49] and for the STM appearance of HOPG. In the following, we present an extensive investigation of how these effects influence the STM imaging of the HOPG surface.

D. Tip-surface interactions and contaminations

As discussed above, the Bardeen approach can only be applied to study tunneling junctions where the interaction between the STM tip and the surface does not cause significant perturbation to both surface and tip.[45,59,63,64] To assess the distance range where the method is safely applicable, we calculated the minimum tip-surface distance to warrant negligible tip-surface perturbation. To this end, two representative W- and C-terminated tip models were optimized at 5.5 Å above the α, β, and h sites of a 7×5 orthorhombic graphene bilayer.[49] We used a semiempirical London approximation to dispersion terms,[72] which proved successful in our recent study of the interactions of metallic tips with relatively large organic molecules with π electrons.[73]

Regardless of the tip-apex position above the surface (α, β, or h site), the calculated out-of-plane deformation (Δz) and the induced change from the equilibrium interlayer distance (Δi) turn out to be smaller than 0.01 Å for a 5.5 Å initial tip height (see Fig. S-7 and Table S-2 in Ref. 49). There is also practically zero electron transfer (Δq) between the tip and surface models. These results indicate negligible interactions and deformations for tip-surface distances $\geqslant$5.5 Å and are in

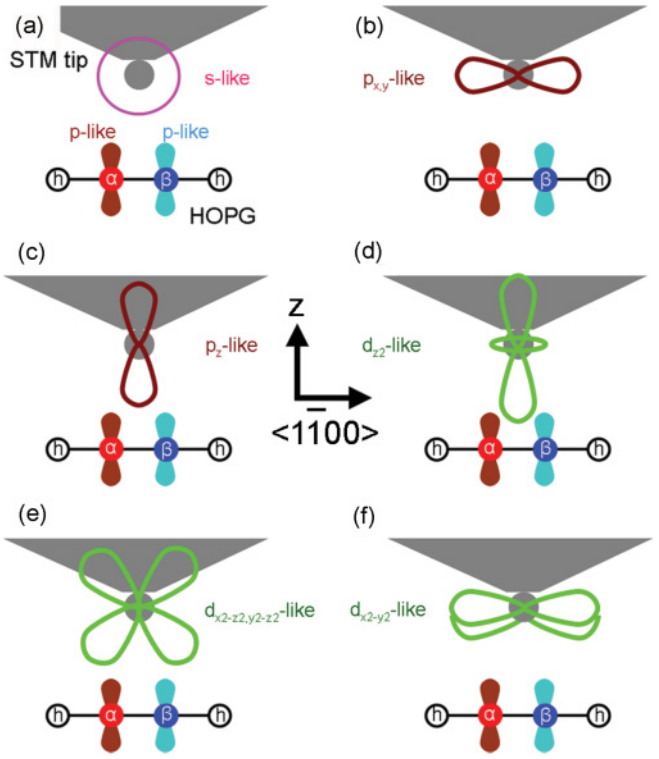

FIG. 7. (Color online) Schematic comparison between the real-space distributions of the HOPG (p) electronic states along $\langle 1\bar{1}00\rangle$ and the different s (a), p [(b), (c)], and d [(d)–(f)] electronic states of the STM tip. The s, p, and d states are indicated on each panel and the HOPG lattice sites are labeled as in Fig. 1(a). See text and Fig. 6 for discussion.

line with the recent results on the interactions between a similar W-tip model and a graphene bilayer obtained with different dispersion corrections.[31] Accordingly, in the following, we will present and discuss only the results of simulations for tip-surface distances $\geqslant$5.5 Å. We expect these results to be representative of STM images acquired in pure tunneling regime.

Finally, we note that the calculated adsorption energy [E_{ads}, Eq. (1)] of the carbon atom at the apex of the W_C tip model is 7.1 eV, i.e., 5.75 eV larger than E_{ads} for the lowest energy configurations of one carbon adatom on the HOPG surface [1.35 eV (Ref. 51)]. Therefore, one can expect contamination of blunt W tip apexes by relatively highly mobile carbon adatoms,[51] especially if the initial stages of tip stabilization are carried out at very close tip-surface distances.

E. Simulated STM imaging of HOPG

1. Tunneling currents

Prior to considering the effects of the tip electronic structure on the constant-current topographic appearance of HOPG, we analyzed also the dependence of the tunneling current on the applied bias for each considered tip model. Based on the different energy-dependent angular- (s,p,d) and magnetic-moment ($x,y,z,xy,xz,yz,x^2-y^2,z^2$) contributions to the tip-apex electronic states (Fig. 6), it is reasonable to expect that the tunneling current may depend also on the relative orientation of the tip and the surface, i.e., on the angle between the projection of the tip apex p (x,y) and d (xy,xz,yz,x^2-y^2) states on the surface plane and the high-symmetry directions of the HOPG sample (Fig. 7). To investigate the extent of such dependence, we considered two orthogonal orientations above the HOPG surface for each tip model. In the first one, the $[1\bar{1}0]$ direction of the W_{sharp}, W_{blunt}, and W_C tip models was oriented parallel to the HOPG $\langle 1\bar{1}00\rangle$ direction (see Fig. 1). In the second one, the tip models were rotated by 90°, which resulted in alignment of the tip [001] and HOPG $\langle 1\bar{1}00\rangle$ directions. From now on, we will refer to the rotated tip models as rW_{sharp}, rW_{blunt}, and rW_C. For compactness of presentation, we will be using the (r)W_{sharp}, (r)W_{blunt}, and (r)W_C notation when simultaneously referring to both the rotated and unrotated W_{sharp}, W_{blunt}, and W_C tip models. While certainly not exhaustive due to the virtually infinite phase space of possible tip structures and orientations, this analysis nevertheless offers qualitative insight into the dependence of the tunneling current and STM contrast on the (experimentally hardly controllable) orientation of the tip-apex atomic structure with respect to the HOPG lattice.

We also recall that at positive biases, electrons tunnel from the tip occupied states to the surface unoccupied states, whereas for negative biases, the tunneling process takes place from the surface occupied states to the tip empty states.[63–65] Figure 8(a) reports the calculated minimum currents for the considered tip models and orientations at a distance of 5.5 Å above the HOPG surface. In all cases, we calculate the current to asymmetrically depend on the bias with larger values for negative biases. Notably, the asymmetry of the calculated I-V curve is found to be larger for the sharp [(r)W_{sharp}] models than for the blunt [(r)W_{blunt}] or C-contaminated [(r)W_C] tips.

Given the symmetric LDOS distribution of the HOPG states [Fig. 5(b)], and the asymmetric LDOS distribution of the tip states [Fig. 6(d)], the calculated I-V behavior originates from the tip electronic structure, specifically from the longer vacuum decay length of the tip empty states with respect to the occupied ones [Fig. 6(d)]. As noted above, this effect is governed by (i) the interplay between fast-decaying in-plane and slow-decaying out-of-plane contributions to the electronic states at the tip apex (Fig. 6); (ii) the contributions of different angular- and magnetic-moment components to the tunneling matrix element [$M_{\tau,n}$ in Eq. (S-4) (Ref. 49)]; and (iii) the convolution effects originating from different in-plane and out-of-plane contributions at the tip apex (Fig. 7).

Consistent with the faster vacuum decay length of C $2p$ electronic states with respect to W $5d$ electronic states (Fig. 6), the calculated currents for the carbon-contaminated tips [(r)W_C] are more than one order of magnitude smaller than for the W-terminated sharp [(r)W_{sharp}] and blunt [(r)W_{blunt}] tip models. Put together, these results clearly indicate that the composition, sharpness, and orientation of the tip apex can substantially affect the tunneling current and its dependence on the applied bias.

2. Corrugation amplitudes

The same parameters strongly affect also the constant-current topographic imaging of HOPG. Figure 8(b) shows the

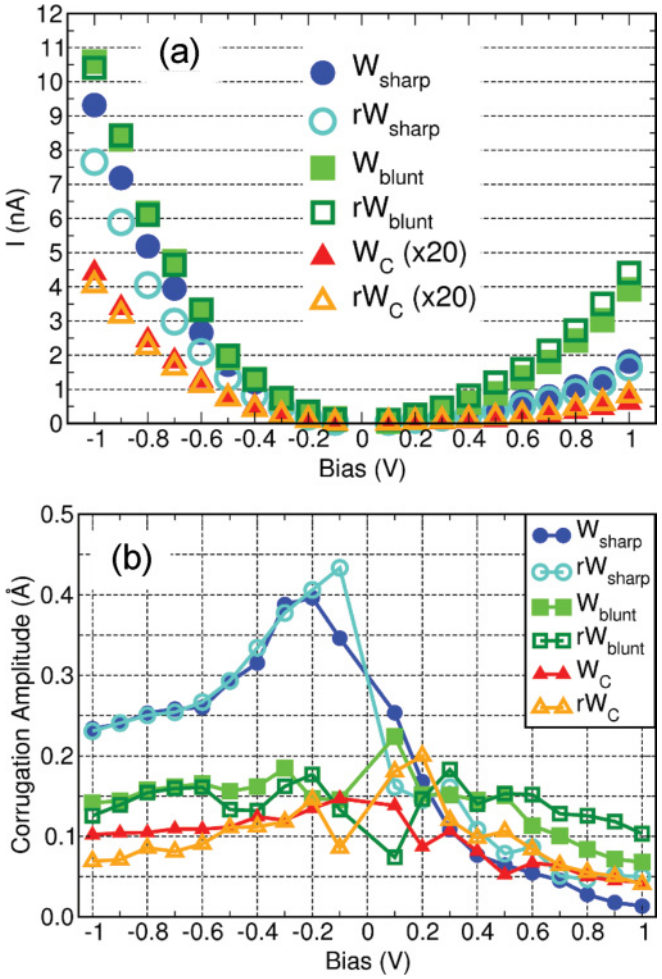

FIG. 8. (Color online) (a) The calculated baseline tunneling currents (nA) as a function of the applied bias (V) for the W_{sharp}, rotated-W_{sharp} (rW_{sharp}), W_{blunt}, rotated-W_{blunt} (rW_{blunt}), C-contaminated (W_C), and rotated-W_C (rW_C) tip models 5.5 Å above the HOPG slab. (b) The calculated corrugation amplitude (Å) at the tunneling I-V conditions in (a) for the considered tip models and orientations.

calculated corrugation amplitude [A, Eq. (S-7) (Ref. 49)] as a function of the applied bias for the considered tip models and orientations at the tunneling I-V conditions of Fig. 8(a). In all cases, we find A to depend on the applied bias and to increase for small biases. While the simulations for the (r)W_{sharp} tips suggest an increase of A for negative biases in-between -0.6 and -0.1 V, the A values calculated with the (r)W_{blunt} and (r)W_C tips peak for small positive biases of 0.1–0.2 V.

Figure 8(b) demonstrates a much stronger effect of the applied bias on the corrugation amplitude for the (r)W_{sharp} models than for other tips. As for the tunneling current, this result stems from the intricate energy-dependent balance between in-plane and out-of plane contributions to the electronic states at the tip apex as determined by both the apex composition and the subapex structure (Fig. 6).

3. *Topographic contrast*

Simulation of the (constant-current) topographic images of HOPG as a function of applied bias allows us to investigate also the effects that different tip terminations can have on the bias dependence of the HOPG contrast. As in the TH case, for compactness of presentation, we present a comparison of the brightness profiles along the $\langle 1\bar{1}00\rangle$ surface direction as calculated from the Bardeen topographic imaging at the tunneling (I,V) conditions reported in Fig. 8(a). The results are presented in Fig. 9 for all the considered tip models and orientations.

Regardless of the tip orientation, the simulations with the blunt tip models [(r)W_{blunt}] yield a topographic contrast in close agreement with TH results. As shown in Figs. 9(c) and 9(d), an increase of the bias beyond ± 0.6 V leads to a progressive conversion of the β-centered triangular pattern into a hexagonal contrast pattern pinned on the α and β atoms. Also in line with TH results, the simulations at biases of different polarity (for instance, $+0.3$ and -0.3 V) lead to practically the same results. Thus, the simulations suggest negligible contrast distortion of the HOPG imaging acquired with W tips of blunt subapex structure.

The sharp [(r)W_{sharp}] tip models show a progressive change from a triangular β-centered structure into a (α- and β-centered) hexagonal pattern for biases more negative than -0.4 V, in qualitative agreement with the TH model for negative biases. However, for positive biases, the results deviate profoundly from the TH predictions. Considering the W_{sharp} tip first, as the positive bias is increased, the contrast repeatedly changes between triangular (0.1–0.2 V, 0.4–0.7 V) and hexagonal (0.3 V, 0.8–1.0 V) patterns. At the same time, the B maximum shifts from the β (α) atoms to mid α-β (h-α) sites. Positive-bias simulations with the rotated rW_{sharp} model give a different deformation of the HOPG contrast with the hexagonal pattern maximum shifted toward the h-α and β-h midpoints for biases of 0.1–0.6 V. Conversely, for biases larger than 0.6 V, the simulated hexagonal B maximum is pinned at the mid α-β and h sites.

Both the contrast change and the shift of the topographic features from the HOPG high-symmetry sites originate from convolution effects (Fig. 7) between the narrowly spaced, fast-decaying $2p$ LDOS of HOPG (Fig. 5) and the blunt (Fig. S-4 in Ref. 49), heterogeneous LDOS at the (r)W_{sharp} apex [Fig. 6(a)]. Given the same in-plane periodicity between the (r)W_{sharp} and (r)W_{blunt} tip models, and the adoption of the same k-point grid to map their electronic structure, we are to conclude that the contrast reversal modeled for the (r)W_{sharp} [but not for (r)W_{blunt}] tip model is not a supercell-induced artifact. Various effects of different tip terminations on the topographic contrast are further illustrated by the results for the carbon-contaminated (r)W_C tip models.

As shown in Figs. 9(e) and 9(f), carbon contamination of the tip apex leads to different deformations of the contrast and, depending on the mutual orientation of the tip subapex and HOPG lattices, to the appearance of hexagonal pattern at small biases (W_C: $-0.1/+0.3$ V), and to the appearance of triangular structures for large negative biases (W_C: $-0.3/-1.0$ V) or positive (W_C: 0.6–1.0 V, rW_C: 0.9–1.0 V) biases. Similar to the (r)W_{sharp} tips, also the (r)W_C-tip simulations suggest that the tip-mediated convolution effects play an important role in shifting the B maxima away from the HOPG high-symmetry sites.

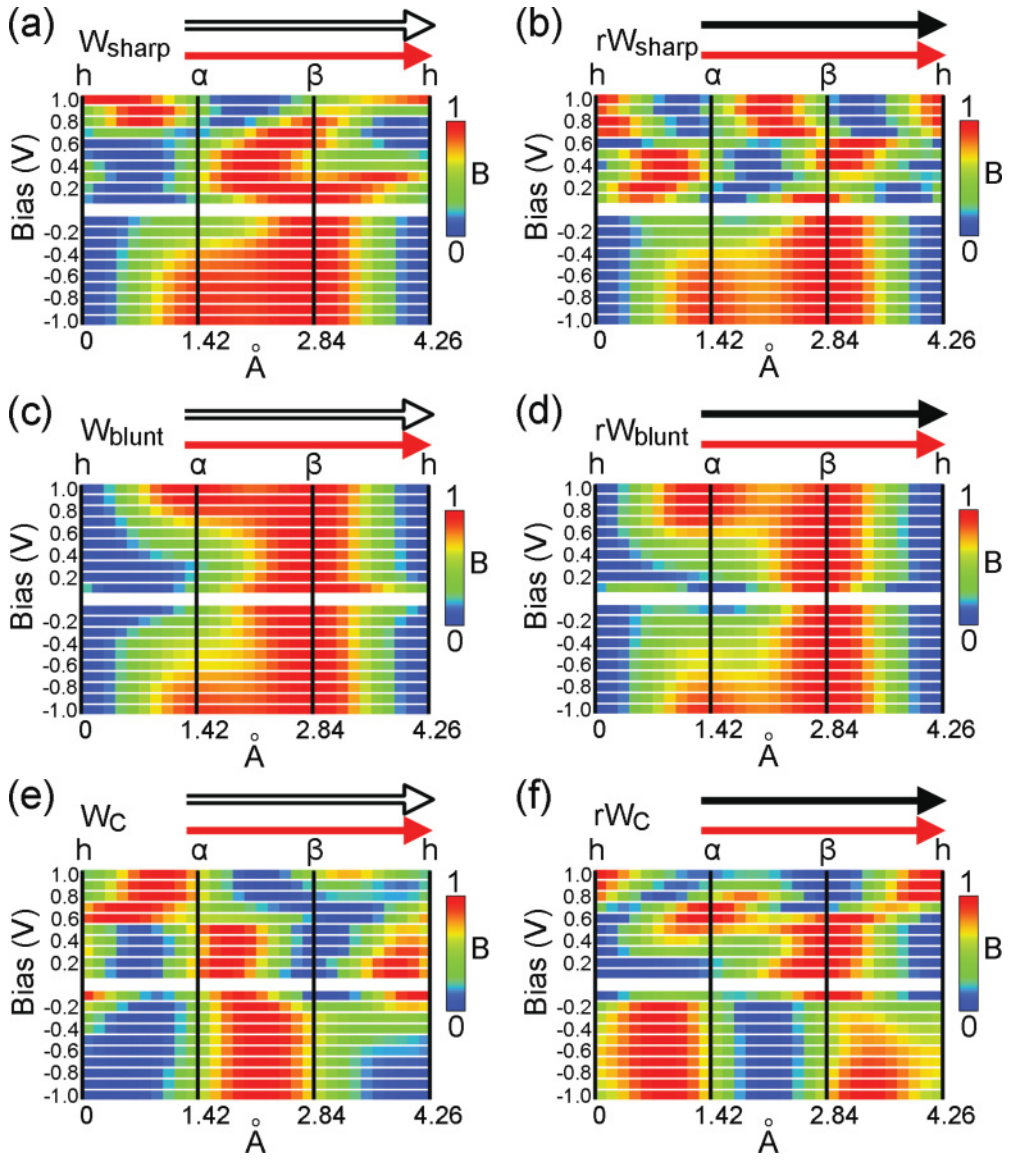

FIG. 9. (Color online) The Bardeen brightness (B) profiles along the $\langle 1\bar{1}00\rangle$ HOPG direction calculated with the W_{sharp} (a), rW_{sharp} (b), W_{blunt} (c), rW_{blunt} (d), W_C (e), and rW_C (f) tip models at the tunneling conditions of Fig. 8(a). The profiles in [(a), (c), and (e)] and [(b), (d), and (f)] have been calculated with the HOPG $\langle 1\bar{1}00\rangle$ direction [red (gray) arrow, see Fig. 1(a)] aligned to the [001] (empty arrows) and $[1\bar{1}0]$ (filled black arrows) tip directions, respectively.

To summarize, these results confirm our earlier observation that different HOPG contrasts obtained in the pure tunneling regime depend on the chemical composition of the tip apex and its subapex structure.

IV. DISCUSSION

In the following, we compare the presented experimental and theoretical results and discuss them in conjunction with the previously published data. To organize the large amount of information presented above, we follow the same structure as in Sec. III by introducing sections on the tunneling currents, the topographic corrugation amplitudes, the topographic contrast, and possible C contamination of the W tips.

A. Constant-height tunneling currents

We start by comparing the measured I-V calibration with previous results acquired at room temperature with W tips. As shown in Fig. 2(a), the experimental I-V calibration exhibits a slightly asymmetric parabolic dependence on the applied bias. This result strongly deviates from the much more asymmetric I-V behavior reported in Ref. 40, where the currents measured for negative biases were larger than for positive biases. The modeled effects of the W-tip sharpness on the asymmetry of the I-V calibration [Fig. 8(a)] suggest that these deviations can be due to a sharper tip termination in Ref. 40 than for the tip adopted here. This would also be consistent with the very long preparation procedure used in our work (see Sec. II), which may have resulted in a relatively blunt yet atomically terminated tip apex.

Despite the evident overestimation of the I-V asymmetry with the (r)W_{sharp} tips, the calculated current values [Fig. 8(a), 10–0.01 nA] semiquantitatively match the present (Fig. 2) and other experimental values.[29,30,34–40,66,67] These results are consistent also with the recent W-tip Bardeen and multiple-scattering simulations of HOPG [∼20 nA at 5 Å (Ref. 31)] performed at a single −0.3 V bias. Crucially, in the latter study, it was also found that multiple-scattering effects (here neglected) do not play any significant role in the STM imaging of HOPG at tip-surface distances larger than 4 Å (or currents smaller than 100 nA). This supports the application of the Bardeen approach to the study of the HOPG appearance in pure tunneling regime.

B. Topographic corrugation amplitudes

To discuss the average corrugation amplitude, we initially note that previous experimental[39] and theoretical studies[23] suggested that a corrugation amplitude (A) smaller than 1.0 Å should be indicative of negligible tip-surface interactions. These indications, combined with the fact that the measured average A values are lower than 1.0 Å [Fig. 2(b)], support our assumption that the tip-surface interaction is indeed negligibly small in the sampled bias range. The only exception is the relatively large 1.3-Å value at −0.2 V [Fig. 2(b)]. Therefore, we attribute the measured changes in corrugation amplitude to bias-related effects.

We note that the bias-dependent A values [0.6–1.3 Å, see Fig. 2(b)] measured here are significantly larger than in one of the previous W-tip investigations of HOPG where A at different biases was always less than 0.1 Å.[39] At the same time, the A value at −0.1 V (0.9 Å) is significantly smaller than that acquired with another W tip (1.5 Å, see Ref. 37). The demonstrated influence of the tip electronic structure on the topographic corrugation amplitude [Fig. 8(b)] suggests that these deviations originate from the unavoidably different tip terminations in the three cases. Given the small and nearly constant (∼0.1 Å) A value for the (r)W_{blunt} tips [see Fig. 8(b)], the simulations point toward a likely blunt termination for the W tip in Ref. 39. At the same time, the marked increase in A for small negative biases with the (r)W_{sharp} models suggests that a sharper tip termination (possibly augmented by some tip-induced surface deformation[23]) could be the origin of the larger ($\geqslant$1.3 Å) A value measured in the present case (at −0.2 V) and at −0.05 V and 0.4 nA in Ref. 37.

C. Topographic contrast

We start by comparing the present results with the available experimental data regarding the dependence of the STM topographic contrast on the applied bias. In line with previous multibias investigations carried out with a W tip,[39] we find that the HOPG contrast can be inverted at positive biases (Fig. 4). Statistically averaged analysis of the corrugation profiles pins the contrast reversals at 0.5 and 0.9 V (Fig. 4). Thus, for intermediate biases in the 0.6–0.9 V range, we recover an apparently standard hexagonal pattern whereby, as for negative biases, the secondary features are always distributed on the left of the primary feature along $\langle 1\bar{1}00\rangle$. These results markedly deviate from the findings of Ref. 39 where an inverted triangular contrast was reportedly measured for biases of 0.5–1.0 V.

On the basis of our simulations (Fig. 9), we attribute this difference to the different tip-preparation schemes (*in situ* tip cleaning by using field emission in Ref. 39, days-long stabilization by repeated scans here), and the ensuing different tip terminations in the two experiments. This is consistent with the predicted strong effects of the tip termination on the HOPG imaging (Fig. 9). It also emphasizes the necessity of having I-V calibrations available (Fig. 2 and Ref. 40) ahead of any meaningful comparison between experimental data sets acquired with different tips.

Prior to turning to the topographic assignment, we note that, unlike the HOPG $\langle 1\bar{1}00\rangle$ direction, the positions of the topographic features in STM images with respect to the HOPG lattice can not be rigorously defined on the basis of the experimental topographies alone (Figs. 3 and 4). However, in analogy with the experimental results, one can safely shift the calculated $\langle 1\bar{1}00\rangle$ scan lines (Fig. 9) to start with the corresponding brightest feature (Fig. 10). Once this is done, it is then possible to directly compare the experimental and calculated scan lines along the (previously assigned) $\langle 1\bar{1}00\rangle$ direction. Provided agreement between the experimental (Fig. 4) and calculated (Fig. 10) shifted data sets exists, this allows assignment of the experimental topographic features to the HOPG lattice sites by reference to the absolute positions of the calculated profiles (Fig. 9). Building on the results of this two-step procedure, we next discuss the topographic assignment of the present and previously published experimental results.

Given the good agreement between the experimental (Fig. 4) and the four calculated [(r)W_{sharp}, (r)W_{blunt}] profiles for negative biases (Figs. 9 and 10), we assign the primary and secondary topographic features to the HOPG β and α atoms, respectively. Accordingly, we conclude that β atoms should be always visible in images acquired with pure W tips at negative biases.

Turning to positive biases, the experimentally measured contrast reversal at 0.5 V is better matched by the results for the W_{sharp} model. The slight underestimation of the contrast-reversal bias (0.2–0.3 V instead of 0.5 V) prevents quantitative agreement with the experiment. However, by taking the 0.2–0.3 V simulations as representative of the experimental (0.5 V) results, it is possible to tentatively assign the bright features at 0.5 V to mid α-β and β-h sites, respectively. Analogously, comparison between the W_{sharp} results (Figs. 9 and 10) and the experimental contrast reversal at 0.9 V (Fig. 4) assigns the experimental hexagonal bright features to mid h-α and β-sites.

These results elucidate the experimentally measured contrast reversal at positive biases as originating from the complex balance between tip-induced convolution effects [Fig.7 and Eq. (S-3) in Ref. 49] and the energy-dependent contribution of tip states with different vacuum decay (Fig. 6). Based on the measurement of different contrast reversals at different biases (Fig. 4 and Ref. 39), and the strong effects of the tip subapex structure on the ensuing HOPG STM contrast (Figs. 9 and 10), we attribute the underestimation of the contrast-bias reversal at 0.5 V (Fig. 4) to differences in experimental and theoretical subapex structures.

More importantly, our simulations clearly suggest that, dependent on the tip composition and structure, different

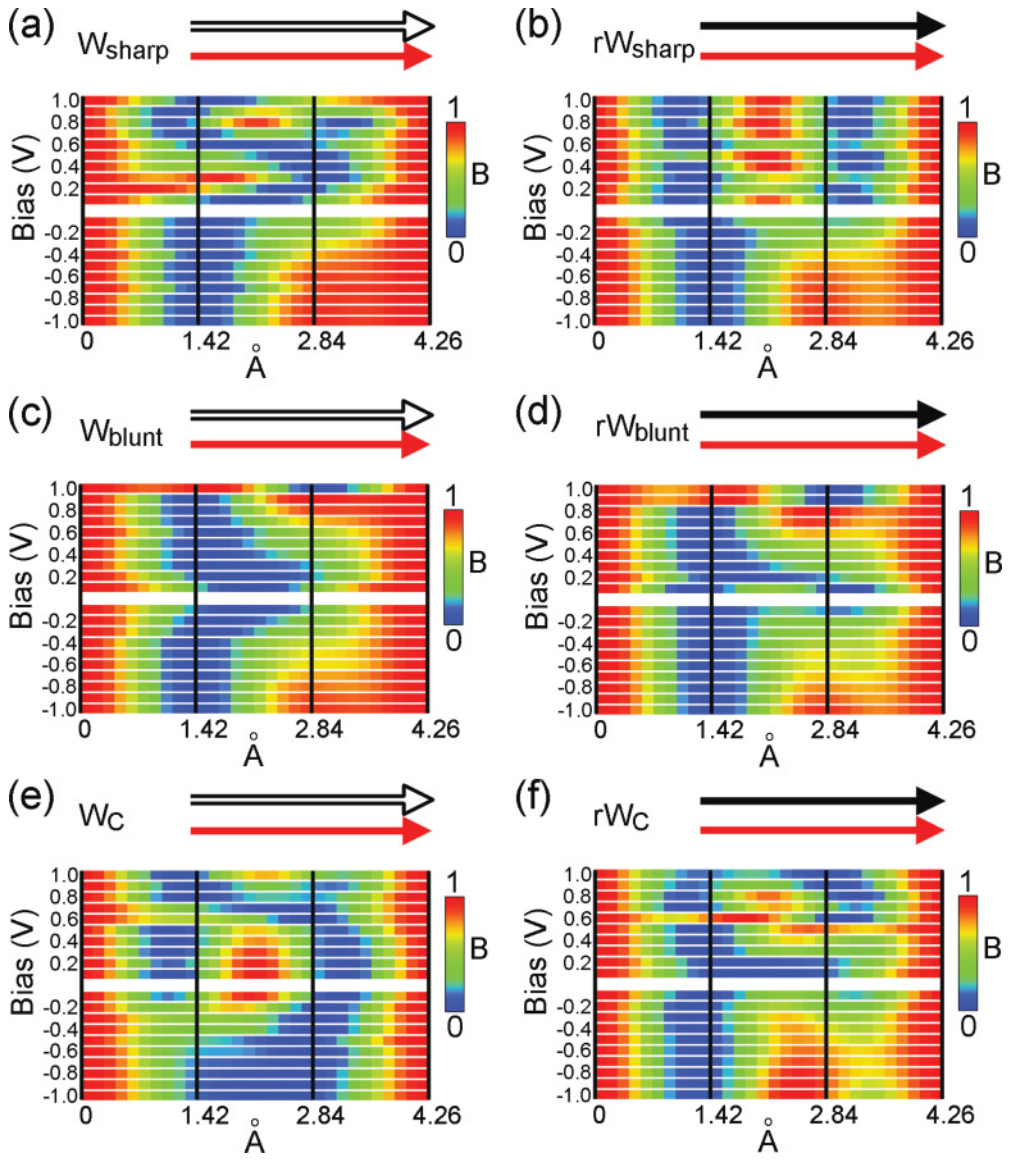

FIG. 10. (Color online) The Bardeen brightness (B) profiles of Fig. 9 arbitrarily shifted to start with the maximum brightness ($B = 1$) position. Same labeling and marks as in Fig. 9. See text and Fig. 4 for discussion.

bias-induced contrast reversals may [(r)W_{sharp}, (r)W_C] or may not [(r)W_{blunt}] be detected. Crucially, these contrast reversals may lead to the appearance of both hexagonal and triangular patterns depending on the particular W tip structure.

These findings provide an understanding and reconciliation of the differences between the experimental results for the HOPG STM imaging. Depending on the tip sharpness and composition, hexagonal (β- and h-centered) structures can be imaged also for small positive biases [rW_{sharp}, Fig. 9(b), and Ref. 37]. Even in the absence of strong tip-surface interactions,[31] hexagonal contrasts at small positive biases may be transformed into a triangular pattern by 1.0 Å retraction of the tip [rW_{sharp}, in Fig. 9(b), and Fig. (S-8b) in Ref. 49]. Moreover, depending of the subapex structure and orientation, triangular contrasts may [W_{sharp}, Fig. 9(a), and Ref. 39] or may not [Fig. 3 and rW_{sharp}, (r)W_{blunt} results in Fig. 9] be obtained for relatively large positive biases of 0.5 –0.7 V.

In this respect, it is interesting to note that none of the simultaneous STM atomic force microscopy (AFM) studies of HOPG employing W tips published to date[38,66,67] have acquired images for biases larger than 0.16 V. Thus, due to the AFM ability to image all the HOPG atoms at relatively large tip-surface distances[31,38,66,67] as considered here, we expect future W-tip STM-AFM investigations at biases exceeding 0.16 V to shed further light on the dependence of the positive-bias HOPG contrast on the instantaneous tip structure (Fig. 9).

Overall, based on the very similar HOPG contrast obtained for the (r)W_{sharp} and (r)W_{blunt} tip models at negative biases (Fig. 9), these should be preferred rather than positive biases for maximally reproducible STM imaging of HOPG with W tips. Under such conditions, and following the presented tip-preparation protocol, it is possible to consistently image the β atoms for biases of $-0.1/-1.0$ V and both the α and β atoms for biases more negative than -0.5 V. Imaging of HOPG at positive biases should be avoided due to the strong

dependence of the STM contrast on the hardly controllable subapex structure and orientation of the tip. Furthermore, stability of the STM contrast for biases of different polarities should be indicative of blunt tip terminations, whereas contrast modifications point toward sharp tips.

Finally, based on the strong dependence of the HOPG positive-bias contrast on the instantaneous tip termination, and the high reproducibility of HOPG samples preparation,[30] we argue that it should be possible to use positive-bias imaging of HOPG and the provided library of contrasts (Figs. 9 and 10) as a standard for the elucidation of the actual tip termination in particular experiments.

D. Identification of C contamination at the tip apex

As shown in Fig. 8, carbon contamination is found to reduce the tunneling current by more than one order of magnitude with respect to pure W tips. Thus, C contamination during constant-height scans can manifest itself as a sudden drop of the tunneling current, or in constant-current topographic scans as a sudden drop of the baseline height.

Additionally, as shown in Figs. 9(e) and 9(f), the (r)W_C models alter the HOPG imaging also at negative biases with respect to W-terminated tips. Thus, C contamination should be also detectable at large negative biases ($-0.7/-1.0$ V) by the appearance of sharp triangular contrast (W_C) or the imaging of hexagonal patterns with anomalously large (>2 Å) separation between the primary and secondary features along $\langle 1\bar{1}00\rangle$ (rW_C).

V. CONCLUSIONS

Our extensive experimental investigation accompanied by statistical analysis of the experimental data set and by first-principles simulations with six different tip models demonstrates a marked effect of the applied bias on the topographic contrast and corrugation amplitude of HOPG acquired with W tips in the pure tunneling regime.

Depending on the applied bias and polarity, both the hexagonal and triangular contrast patterns can be imaged with the same stable tip. Statistical analysis of the experimental data set reveals enhancement of the corrugation amplitude for small negative biases and the occurrence of different contrast reversals at positive biases, whereby the relative brightness of the primary and secondary features is inverted with respect to the negative-biases results. Simulation of HOPG imaging with different tip models provides better understanding of these findings and demonstrates the profound effects of the tip electronic structure on the measured HOPG imaging.

For pure W tips, regardless of the tip structure and orientation, the negative-bias contrast is shown to progressively change from a β-centered triangular pattern into a hexagonal pattern pinned on α and β atoms for biases more negative than -0.5 V. Conversely, the positive-bias contrast is found to strongly depend on the tip structure, sharpness, and orientation with respect to the HOPG lattice. Whereas blunt tip terminations yield the same contrast for both bias polarities, sharper tips profoundly distort the HOPG imaging at positive biases. These results originate from tip-convolution effects, which in turn depend on the intricate balance between electronic states of different angular and magnetic moments and their different vacuum decay length outside the tip apex.

The simulations suggest that STM acquisition at negative biases should be preferred with W tips as this leads to more reproducible imaging of HOPG. On the same grounds, and given the high reproducibility of HOPG sample preparation, it is argued that positive-bias imaging of HOPG could be used, together with the presented library of contrasts, as a way of determining the actual tip termination. Carbon contamination of the W tip is shown to make the HOPG contrast to strongly depend on the tip termination also for negative biases. This, together with the corresponding reduction in the tunneling current, can be used for identifying or ruling out carbon contamination of the W tip during the STM acquisition.

Overall, these results highlight elements so far overlooked, which should be useful for the interpretation of the exceedingly large number of STM images of HOPG, and technologically relevant related systems such as nanoengineered HOPG, multilayer graphene, graphite-supported biomolecules, and catalysts. Finally, the introduced experimental protocol for the tip preparation and calibration, together with the statistical analysis of the ensuing results, opens up for a more straightforward and rigorous comparison between STM images acquired with different tips.

ACKNOWLEDGMENTS

This work was supported by a specially promoted Grant-in-Aid for Scientific Research (Contract No. 19001002) from the Ministry of Education, Culture, Sports, Science and Technology (MEXT) of Japan, and by World Premier International Research Center Initiative (WPI), MEXT, Japan. The authors also acknowledge the use of the UCL Legion High Performance Computing Facility, and associated support services, in the completion of this work. G.T. is currently supported by EPSRC-UK (EP/I004483/1). G.T. is grateful to W. A. Hofer for useful discussion.

*g.teobaldi@liv.ac.uk
†tanimura@sanken.osaka-u.ac.jp
‡a.shluger@ucl.ac.uk

[1] W.-T. Pong and C. Durkan, J. Phys. D: Appl. Phys. **38**, R329 (2005).
[2] R. C. Tatar and S. Rabii, Phys. Rev. B **25**, 4126 (1982).
[3] B. T. Kelly, *Physics of Graphite* (Applied Science, London 1981).
[4] H. J. Mamin, E. Ganz, D. W. Abraham, R. E. Thomson, and J. Clarke, Phys. Rev. B **34**, 9015 (1986).
[5] H. Shinohara, Rep. Prog. Phys. **63**, 843 (2000).
[6] S. De Feyter and F. C. De Schryver, Chem. Soc. Rev. **32**, 139 (2003).
[7] C. R. Clemmer and T. P. Beebe, Scanning Microsc. **6**, 319 (1992).
[8] J. Otsuki, Coord. Chem. Rev. **254**, 2311 (2010).
[9] M. Ruben, J.-M. Lehn, and P. Müller, Chem. Soc. Rev. **35**, 1056 (2006).
[10] H. Hövel and I. Barke, Prog. Surf. Sci. **81**, 53 (2006).

[11] M. Lenner, A. Kaplan, and R. E. Palmer, Appl. Phys. Lett. **90**, 153119 (2007).
[12] J. Kanasaki, E. Inami, K. Tanimura, H. Ohnishi, and K. Nasu, Phys. Rev. Lett. **102**, 087402 (2009).
[13] J. I. Paredes, A. Martinez-Alonso, and J. M. D. Tascón, Carbon **38**, 1183 (2000).
[14] J. I. Paredes, P. Solís-Fernández, A. Martinez-Alonso, and J. M. D. Tascón, J. Phys. Chem. C **113**, 10249 (2009).
[15] K. H. Han, D. Spemann, P. Esquinazi, R. Höhne, V. Riede, and T. Butz, Adv. Mater. **15**, 1719 (2003).
[16] Y. Ferro, C. Thomas, T. Angot, P. Génésio, and A. Allouche, J. Nucl. Mater. **363–365**, 1206 (2007).
[17] M. J. Allen, V. C. Tung, and R. B. Kaner, Chem. Rev. **110**, 132 (2010).
[18] T. W. Odom, J.-L. Huang, P. Kim, and C. M. Lieber, Nature (London) **391**, 62 (1998).
[19] J. W. G. Wilder, L. C. Venema, A. G. Rinzler, R. E. Smallery, and C. Dekker, Nature (London) **391**, 59 (1998).
[20] Y. Z. Li, J. C. Patrin, M. Chander, J. H. Weaver, L. P. F. Chibante, and R. E. Smallery, Science **252**, 447 (1991).
[21] P. Lauffer, K. V. Emtsev, R. Graupner, Th. Seyller, L. Ley, S. A. Reshanov, and H. B. Weber, Phys. Rev. B **77**, 155426 (2008).
[22] R. Hiesgen, I. Wehl, E. Aleksandrova, E. Roduner, A. Bauder, and K. A. Friedrich, Int. J. Energy Res. **34**, 1223 (2010).
[23] J. M. Soler, A. M. Baro, N. Garcia, and H. Rohrer, Phys. Rev. Lett. **57**, 444 (1986).
[24] J. B. Pethica, Phys. Rev. Lett. **57**, 3235 (1986).
[25] M. Kuwabara, D. R. Clarke, and D. A. Smith, Appl. Phys. Lett. **56**, 2396 (1990).
[26] J. Xhie, K. Sattler, M. Ge, and N. Venkateswaran, Phys. Rev. B **47**, 15835 (1993).
[27] W.-T. Pong, J. Bendall, and C. Durkam, Surf. Sci. **601**, 498 (2007).
[28] E. Cisternas, M. Flores, and P. Vargas, Phys. Rev. B **78**, 125406 (2008).
[29] S. I. Park and C. F. Quate, Appl. Phys. Lett. **48**, 112 (1986).
[30] G. Bining, H. Fuchs, Ch. Gerber, H. Rohrer, E. Stoll, and E. Tosatti, Europhys. Lett. **1**, 31 (1986).
[31] M. Ondráček, P. Pou, V. Rozsíval, C. González, P. Jelínek, and R. Pérez, Phys. Rev. Lett. **106**, 176101 (2011).
[32] P. Moriarty and G. Hughes, Appl. Phys. Lett. **60**, 2338 (1992).
[33] H. A. Mizes, S. I. Park, and W. A. Harrison, Phys. Rev. B **36**, 4491 (1987).
[34] P. J. Ouseph, T. Poothackanal, and G. Mathew, Phys. Lett. A **205**, 65 (1995).
[35] J. I. Paredes, A. Martínez-Alonso, and J. M. D. Tascón, Carbon **39**, 476 (2001).
[36] Y. Wang, Y. Ye, and K. Wu, Surf. Sci. **600**, 729 (2006).
[37] E. Cisternas, F. Stavale, M. Flores, C. A. Achete, and P. Vargas, Phys. Rev. B **79**, 205431 (2009).
[38] S. Hembacher, F. J. Giessibl, J. Mannhart, and C. F. Quate, Proc. Natl. Acad. Sci. USA **100**, 12539 (2003).
[39] S. Gwo and C. K. Shih, Phys. Rev. B **47**, 13059 (1993).
[40] G. S. Khara and J. Choi, J. Phys.: Condens. Matter **21**, 195402 (2009).
[41] D. Tománek, S. G. Louie, H. J. Mamin, D. W. Abraham, R. E. Thomson, E. Ganz, and J. Clarke, Phys. Rev. B **35**, 7790 (1987).
[42] D. Tománek and S. G. Louie, Phys. Rev. B **37**, 8327 (1988).
[43] J. Tersoff, Phys. Rev. B **41**, 1235 (1990).
[44] J. Tersoff and N. D. Lang, Phys. Rev. Lett. **65**, 1132 (1990).
[45] N. Isshiki, K. Kobayashi, and M. Tsukada, Surf. Sci. Lett. **238**, L439 (1990).
[46] A. Selloni, P. Carnevali, E. Tosatti, and C. D. Chen, Phys. Rev. B **31**, 2602 (1985).
[47] C. D. Zeinalipour-Yazdi and D. P. Pullman, Chem. Phys. **348**, 233 (2008).
[48] J. Tersoff and D. R. Hamann, Phys. Rev. B **31**, 805 (1985).
[49] See Supplemental Material at http://link.aps.org/supplemental/10.1103/PhysRevB.85.085433 for supplementary methods and results.
[50] R. K. Raman, Y. Murooka, C. Y. Ruan, T. Yang, S. Berber, and D. Tománek, Phys. Rev. Lett. **101**, 077401 (2008).
[51] G. Teobaldi, K. Tanimura, and A. L. Shluger, Phys. Rev. B **82**, 174104 (2010).
[52] G. Teobaldi, H. Ohnishi, K. Tanimura, and A. L. Shluger, Carbon **48**, 4145 (2010).
[53] A. Bosak, M. Krisch, M. Mohr, J. Maultzsch, and C. Thomsen, Phys. Rev. B **75**, 153408 (2007).
[54] G. Teobaldi, W. A. Hofer, O. Bikondoa, C. L. Pang, G. Cabailh, and G. Thornton, Chem. Phys. Lett. **437**, 73 (2007).
[55] G. Teobaldi, M. Peñalba, A. Arnau, N. Lorente, and W. A. Hofer, Phys. Rev. B **76**, 235407 (2007).
[56] J. P. Perdew, K. Burke, and M. Ernzerhof, Phys. Rev. Lett. **77**, 3865 (1996).
[57] G. Kresse and J. Hafner, Phys. Rev. B **47**, 558 (1993).
[58] G. Kresse and J. Furthmüller, Phys. Rev. B **54**, 11169 (1996).
[59] J. Bardeen, Phys. Rev. Lett. **6**, 57 (1961).
[60] W. Hofer and J. Redinger, Surf. Sci. **447**, 51 (2000).
[61] W. A. Hofer, Prog. Surf. Sci. **71**, 147 (2003).
[62] K. Palotas and W. A. Hofer, J. Phys.: Condens. Matter **17**, 2705 (2005).
[63] W. A. Hofer, A. S. Foster, and A. L. Shluger, Rev. Mod. Phys. **75**, 1287 (2003).
[64] J. M. Blanco, C. Gonzalez, P. Jelínek, J. Ortega, F. Flores, and R. Pérez, Phys. Rev. B **70**, 085405 (2004).
[65] M. Tsukada, K. Kobayashi, N. Isshiki, and H. Kageshima, Surf. Sci. Rep. **13**, 265 (1991).
[66] S. Hembacher, F. J. Giessibl, J. Mannhart, and C. F. Quate, Phys. Rev. Lett. **94**, 056101 (2005).
[67] S. Kawai and H. Kawakatsu, Phys. Rev. B **79**, 115440 (2009).
[68] F. Atammy, O. Spilleche, and R. Schlogl, Phys. Chem. Chem. Phys. **1**, 4113 (1999).
[69] B. Partoens and F. M. Peeters, Phys. Rev. B **74**, 075404 (2006).
[70] P. R. Wallace, Phys. Rev. **71**, 622 (1947).
[71] W. A. Hofer, J. Redinger, and P. Varga, Solid State Commun. **113**, 245 (2000).
[72] F. Ortmann, F. Bechstedt, and W. G. Schmidt, Phys. Rev. B **73**, 205101 (2006).
[73] K. Lämmle, T. Trevethan, A. Schwarz, M. Watkins, A. L. Shluger, and R. Wiesendanger, Nano Lett. **10**, 2965 (2010).